HCMT models of optical microring-resonator circuits

*Manfred Hammer**

MESA$^+$ Institute for Nanotechnology, University of Twente, Enschede, The Netherlands

Abstract: Circuits of dielectric integrated optical microring resonators are addressed through a 2-D hybrid analytical / numerical coupled mode theory (HCMT) model. Analytical modes of all straight and curved cores form templates for the optical fields of the entire circuits. Our variational technique then generates solutions for the amplitude functions in their natural Cartesian and polar coordinates, discretized by 1-D finite elements. Bidirectional wave propagation through all channels and pronounced reflections can be taken into account. The series of examples includes rings coupled in parallel, rows of cavities (coupled resonator optical waveguides, CROWs) of varying length, a triangular photonic molecule, and a resonator with a slit ring to illustrate the role of intra-cavity reflections.

Keywords: Optical microring-resonators, numerical / analytical modeling, coupled mode theory.

PACS codes: 42.82.–m 42.82.Bq 42.82.Et

1 Introduction

The variants of dielectric optical micro-ring resonators, and circuits made thereof, are already for some time discussed as promising concepts in integrated optics, e.g. for applications in optical telecommunications or optical sensing. See [1, 2] for recent overviews of the field. Frequently these structures tend to be inconvenient when it comes to rigorous numerical simulations: Compared to other photonic circuits they typically cover larger areas, i.e. require larger computational windows on which the optical waves have to be represented adequately, such that also local mesh refinement does not help much. At the same time, fine spectral details need to be resolved, either by detailed wavelength scans of a frequency domain solver, or by long integration intervals in case of time domain calculations.

As a more viable alternative, approaches based on coupled mode theory (CMT) are quite popular. Mostly these are parametric models [3, 4, 5, 6] that combine scattering matrices for the coupler regions and effective indices for the wave propagation along the connecting channels into analytic descriptions. Explicit solutions are obtainable for simpler, typically highly symmetric structures, used also for fitting experimental data [7, 8, 9]. Coupling constants and transmission coefficients of the couplers, sometimes also the phase propagation and attenuation constants of the cavity modes are treated as free (fit) parameters.

Attempts to determine values for these parameters from first principles, i.e. by solving the coupled mode equations [10, 11] for the evanescent wave interaction in the coupler regions, are seen less often. Examples are found in [12, 13], more recently in [14], the latter formulation has also led to a 3-D implementation [15]. These first-principle CMT descriptions of microring circuits, however, require specific localized interaction regions with (more or less) well defined outlets that need to be carefully stitched together by analytic expressions for the wave propagation along the connecting straight and bent channels within a scattering matrix formalism. Inside the coupler regions, the coupled mode equations are usually written for a single propagation coordinate, which appears to be decidedly unnatural e.g. in case of the evanescent wave interaction between adjacent straight and bent channels.

As an alternative we propose to apply the Hybrid analytical / numerical Coupled Mode Theory (HCMT) formalism of [16, 17]. The approach can treat directly the full resonator circuits, i.e. avoids the necessity to identify spatially distinct regions of interaction, and to establish scattering matrices for carefully defined input/output ports (although a restriction to coupler regions would certainly be possible just as well). Each of the interacting waves can be described with its natural coordinates of propagation. Once the computer code exists, the method turns out to be quite versatile and easily applicable.

We consider optical microresonator circuits that consist of a number of not necessarily identical circular cavities and straight waveguides, with evanescent wave interaction between these elements. The standard configuration

---

* *Department of Electrical Engineering, University of Twente*   *P.O. Box 217, 7500 AE Enschede, The Netherlands*
Phone: +31/53/489-3448   *Fax: +31/53/489-3996*   *E-mail: m.hammer@ewi.utwente.nl*

of Figure 1 serves as an example. Given the analytical modes of the two bus cores and the bend mode(s) [10, 18, 19] supported by the curved waveguide profile that constitutes the cavity, one readily writes an ansatz for the time harmonic electromagnetic field, using the natural Cartesian and polar coordinates for the straight and curved waveguide elements. In line with the HCMT approach [16] the unknown amplitudes (functions) of the given mode profiles are discretized by linear 1-D finite elements over suitable coordinate intervals. Then a Galerkin procedure is applied on a computational window that covers the entire resonator circuit. One obtains a dense, but small size algebraic system of equations for the element coefficients. The numerical solution yields approximations for the amplitude functions and permits to reassemble the overall optical field.
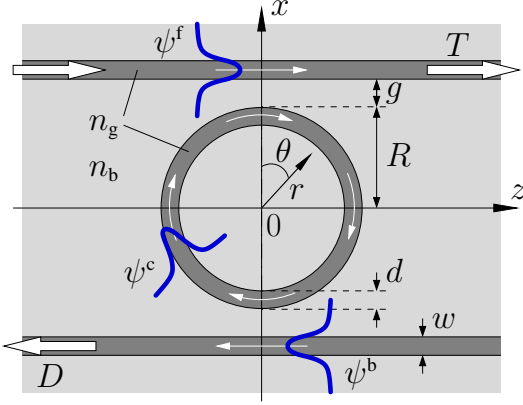

Figure 1: A circular cavity between two bus channels, unidirectional HCMT model, schematically. Guided light enters from the left through the upper core; interest is in the relative transmitted and dropped guided optical powers T and D, and in their spectral properties. Ringresonator functionality is established by the evanescent interaction of the directional guided modes ψ_f, ψ_b associated with the bus channels and the bend mode ψ_c supported by the cavity core. Cartesian coordinates x, z and polar coordinates r, θ will be used. Parameters: cavity radius $R = 7.5\,\mu$m (outer rim), width of the cavity ring $d = 0.75\,\mu$m, waveguide width $w = 0.6\,\mu$m, gap between ring and bus waveguides $g = 0.3\,\mu$m, refractive index of all guiding regions $n_g = 1.5$, of the background $n_b = 1.0$, target vacuum wavelength $\lambda \approx 1.56\,\mu$m.

So far the implementation [20, 21] is restricted to two spatial dimensions and to TE polarization. The parameters as introduced in the figure caption apply analogously to all further structures in this paper, unless other values are given. We thus focus on an intermediate regime with small, but not too tiny cavities with substantial, but not too large refractive index contrast, where a coupled mode approach has some chance to work well, while rigorous numerical schemes (e.g. the popular FDTD simulations) are already inconveniently computationally expensive, even in the 2D case, at least for the larger circuits of Sections 4 and 6.

The outline of the model in Section 2 closes with a section on the efficient evaluation of spectral properties. The approach covers quite general multi-cavity configurations with unidirectional as well as bidirectional wave propagation through all elements, as illustrated by the examples in Sections 3 – 7.

2   Hybrid analytical / numerical coupled mode theory

The approach will be outlined along the example of Figure 1. More involved configurations with multiple guided modes in each channel and/or with bidirectional mode propagation along the cores can be handled analogously with a correspondingly extended field template. Also the adaptation to structures with more and quite arbitrarily positioned channels is straightforward. Further details of the theory, including an alternative truly variational formulation, can be found in [16].

2.1   HCMT field template

Starting point is a plausible and convenient template for the overall electromagnetic field in the form of a superposition of known fields. Typically these are the guided modes supported by the optical channels in the structure with amplitudes that are functions of suitable propagation coordinate(s).

For the single ring resonator, according to Figure 1, one identifies the following basis elements. Light propagates along the bus channels in the form of the directional modes

$$\boldsymbol{\psi}^{\mathrm{f,\,b}}(x, z) = \begin{pmatrix} \tilde{\boldsymbol{E}} \\ \tilde{\boldsymbol{H}} \end{pmatrix}^{\mathrm{f,\,b}} (x)\, \mathrm{e}^{\mp \mathrm{i}\beta z}. \tag{1}$$

$\boldsymbol{\psi}^{\mathrm{f,\,b}}$ covers the six electromagnetic components $\tilde{\boldsymbol{E}}^{\mathrm{f,b}}$, $\tilde{\boldsymbol{H}}^{\mathrm{f,b}}$ of the mode profile, together with the exponential dependence on the propagation distance z with phase constants $-\beta$ (forward propagation $^{\mathrm{f}}$, upper waveguide)

and $+\beta$ (backward propagation [b], lower waveguide). We assume a time dependence $\sim \exp(\mathrm{i}\omega t)$ of all time harmonic fields, with the frequency ω specified by the wavelength $\lambda = 2\pi\mathrm{c}/\omega$, for vacuum speed of light c.

Waves travel around the cavity in the form of the clockwise propagating bend mode

$$\boldsymbol{\psi}^{\mathrm{c}}(r, \theta) = \begin{pmatrix} \tilde{\boldsymbol{E}} \\ \tilde{\boldsymbol{H}} \end{pmatrix}^{\mathrm{c}}(r)\, \mathrm{e}^{-\mathrm{i}\gamma R\theta}, \tag{2}$$

given in polar coordinates by the radial dependent bend mode profile $\tilde{\boldsymbol{E}}^{\mathrm{c}}$, $\tilde{\boldsymbol{H}}^{\mathrm{c}}$ and the complex angular propagation constant γ. Note that the value of γ depends on the definition of the cavity radius R [6], which here represents the outer rim of the cavity.

A superposition of the three former expressions then constitutes the template for the overall electromagnetic field $\boldsymbol{E}$, $\boldsymbol{H}$,

$$\begin{pmatrix} \boldsymbol{E} \\ \boldsymbol{H} \end{pmatrix}(x, z) = f(z)\, \boldsymbol{\psi}^{\mathrm{f}}(x, z) + b(z)\, \boldsymbol{\psi}^{\mathrm{b}}(x, z) + c(\theta)\, \boldsymbol{\psi}^{\mathrm{c}}(r, \theta), \tag{3}$$

with as of yet unknown amplitudes $f(z)$, $b(z)$, $c(\theta)$, each a function of one variable. The formal relation $r = r(x, z)$, $\theta = \theta(x, z)$ between the polar and Cartesian coordinates is to be understood implicitly for Eq. (3) to make sense, but will be taken into account explicitly only at a later stage.

With the non-integer exponent γR, the cavity part (2) of Eq. (3) exhibits a discontinuity at $\theta = 0, 2\pi$. While in principle this jump could be compensated by an equally discontinuous amplitude c, we prefer to remove the phase mismatch after one round trip and the decay in amplitude of the bend mode from the fixed part of the template. The factor $\exp(-\mathrm{i}\gamma R\theta)$ in Eq. (2) is thus replaced by $\exp(-\mathrm{i}\kappa R\theta)$ with a real constant

$$\kappa = \mathrm{floor}(\mathrm{Re}\gamma R + 1/2)/R \tag{4}$$

(here $\mathrm{floor}(x)$ is the largest integer smaller than x) such that κR is an integer number that resembles as good as possible the rapid angular phase gain of the bend mode. Any further phase variations as well as local variations in absolute amplitude (also the bend mode losses) can be covered by a smooth, prospectively slowly varying complex function c that is also smooth (i.e. continuous with continuous derivative) at the transition $2\pi \to 0$.

One should be aware that the template (3) determines which physical effects are covered by the simulations. For the present circuits, this concerns in particular the optical losses. Losses due to the bend mode propagation along the ring are well taken into account, as is clearly visible in the spectra of e.g. Figure 4, where the dropped and transmitted power do not add up to one in general. Other loss mechanisms, e.g. radiation related to the wave interaction in the coupler regions, are disregarded by our models.

2.2 HCMT procedure

It remains to determine the three functions f, b, and c. Analytical solutions are not to be expected for the present system anyway, hence we continue directly with numerical means. For the amplitude f of the forward wave in the upper core a straightforward finite element (FE) discretization reads

$$f(z) = \sum_{j=0}^{N} f_j\, \alpha_j(z). \tag{5}$$

Here the α_j are (in the simplest case) the standard triangular functions associated with an equidistant 1-D first order finite element discretization over a finite interval of the z-axis, with half infinite first and last elements (cf. [16] for explicit expressions). Analogous discretizations are applied to $b(z)$ and $c(\theta)$, where for the latter the first and last elements on the interval $\theta \in [0, 2\pi]$ are identified. Note that the amplitude $c(\theta)$ of the cavity mode is discretized into finite elements first; the formal transformation to Cartesian coordinates follows thereafter. After this step we are left with the task to find values for the now discrete coefficients f_j, b_j, and c_j.

With dots as wildcards for indices and arguments, the template (3) can now be written in the generic form

$$\begin{pmatrix} \boldsymbol{E} \\ \boldsymbol{H} \end{pmatrix}(x,z) = \sum_k a_k \left(\alpha_{\cdot}(\cdot) \boldsymbol{\psi}^{\cdot}(\cdot,\cdot) \right) =: \sum_k a_k \begin{pmatrix} \boldsymbol{E}_k \\ \boldsymbol{H}_k \end{pmatrix}(x,z), \tag{6}$$

where the symbolic index k covers the summation over the different channels, the possibly multiple modes in each channel, and the element indices of each individual FE discretization. The "modal elements" $(\boldsymbol{E}_k, \boldsymbol{H}_k)$ consist of the mode fields (1), (2), multiplied by the respective FE triangle functions. All former coefficients are combined into one set of variables $a_k \in \{f_j, b_j, c_j\}$. Most of these are unknowns, but some represent given quantities: A value one for the coefficient of the first, half-infinite element of f realizes a guided wave input with unit amplitude in the upper left port. The zero value of the coefficient for the last element in the discretization of b suppresses any input from the right in the lower channel.

As the next step we establish a system of equations for the a_k through a Galerkin projection procedure. Solutions of the Maxwell curl equations for the frequency domain

$$\boldsymbol{\nabla} \times \boldsymbol{H} - \mathrm{i}\omega\epsilon_0\epsilon\boldsymbol{E} = 0, \qquad -\boldsymbol{\nabla} \times \boldsymbol{E} - \mathrm{i}\omega\mu_0\boldsymbol{H} = 0 \tag{7}$$

are to be approximated as good as the template (3) permits. $\epsilon(x,z)$ here represents the relative dielectric permittivity of the full structure, ϵ_0 and μ_0 are the vacuum permittivity and permeability, respectively.[1] Multiplication of Eqs. (7) by test fields $\boldsymbol{E}'$ and $\boldsymbol{H}'$ and integration over a suitable computational domain Ω leads to a weak form of Eqs. (7):

$$\iiint_\Omega \mathcal{K}(\boldsymbol{E}',\boldsymbol{H}';\boldsymbol{E},\boldsymbol{H}) \, \mathrm{d}x \, \mathrm{d}y \, \mathrm{d}z = 0 \quad \text{for all } \boldsymbol{E}', \ \boldsymbol{H}', \tag{8}$$

with

$$\mathcal{K}(\boldsymbol{E}',\boldsymbol{H}';\boldsymbol{E},\boldsymbol{H}) = (\boldsymbol{E}')^* \cdot (\boldsymbol{\nabla} \times \boldsymbol{H}) - (\boldsymbol{H}')^* \cdot (\boldsymbol{\nabla} \times \boldsymbol{E}) - \mathrm{i}\omega\epsilon_0\epsilon(\boldsymbol{E}')^* \cdot \boldsymbol{E} - \mathrm{i}\omega\mu_0(\boldsymbol{H}')^* \cdot \boldsymbol{H} \,. \tag{9}$$

One now inserts the template (3) for $\boldsymbol{E}$, $\boldsymbol{H}$, restricts the test fields to the modal elements $\boldsymbol{E}_l$, $\boldsymbol{H}_l$, and thus obtains the linear set of equations

$$\sum_k K_{lk} a_k = 0, \quad \text{with} \quad K_{lk} = \iiint_\Omega \mathcal{K}(\boldsymbol{E}_l, \boldsymbol{H}_l; \boldsymbol{E}_k, \boldsymbol{H}_k) \, \mathrm{d}x \, \mathrm{d}y \, \mathrm{d}z \,. \tag{10}$$

To proceed, the vector of coefficients $\boldsymbol{a} = (a_k)$ and accordingly the matrix $\mathsf{K} = (K_{lk})$ are rearranged and split to separate unknowns $\boldsymbol{u}$ and given quantities $\boldsymbol{g}$, such that the system can be given the form

$$\begin{pmatrix} \mathsf{K}_{uu} & \mathsf{K}_{ug} \\ \mathsf{K}_{gu} & \mathsf{K}_{gg} \end{pmatrix} \begin{pmatrix} \boldsymbol{u} \\ \boldsymbol{g} \end{pmatrix} = 0, \text{ or } \mathsf{K}_u\boldsymbol{u} = -\mathsf{K}_g\boldsymbol{g} \text{ with } \mathsf{K}_u = \begin{pmatrix} \mathsf{K}_{uu} \\ \mathsf{K}_{gu} \end{pmatrix}, \quad \mathsf{K}_g = \begin{pmatrix} \mathsf{K}_{ug} \\ \mathsf{K}_{gg} \end{pmatrix}. \tag{11}$$

The unknowns in the — overdetermined — linear system of equations are finally found in a least squares sense as the solution of

$$\mathsf{K}_u^\dagger \mathsf{K}_u \boldsymbol{u} = -\mathsf{K}_u^\dagger \mathsf{K}_g \boldsymbol{g} \,. \tag{12}$$

Here † denotes the adjoint. See [16] for a further discussion of the procedures, and for alternative schemes.

For purposes of notational compactness the above outline has been given for a 3-D configuration. After restricting the model to TE polarized waves in the 2-D x-z-plane, only the transverse electric component E_y and the two in-plane magnetic components H_x and H_z of all fields remain; the y-integration in all integral expressions is dropped. It is then straightforward to write out the kernel (9) explicitly in components.

---

[1] The fields ψ^{f}, ψ^{b}, ψ^{c} that constitute the template (3) satisfy formally the same equations, but each with different permittivity functions that represent the upper core, the lower core, or the cavity only, always on a homogeneous background.

2.3 Fast evaluation of spectral properties

Frequently one is interested in spectral properties, i.e. in scans over the wavelength parameter λ. Unfortunately in the frequency domain formulation given so far almost all quantities are wavelength dependent. Hence in principle one would have to repeat the entire procedure as discussed before for every new sample wavelength. This may become quite cumbersome even for the present 2-D configurations, in particular if fine spectral details around some resonance features need to be resolved. A way out is found in the following observations.

At least for the moderately low numbers of unknowns that play a role here, the most time consuming part of the simulations is the evaluation of the "overlaps" K_{lk} in Eq. (10), which in principle needs to be repeated for each new wavelength sample point. For a reasonably narrow wavelength interval, say a couple of free spectral ranges of a not-too small resonator, one can expect, however, that the properties of the modal basis fields change but slowly with λ, while rapid spectral variations are due to the *solution* of the linear system involving K.

Consequently, in order to reduce the numerical effort, one might be tempted to restrict the actual computation of $K(\lambda)$ to a few suitably selected sample points, say $\lambda_0 := (3\lambda_a + \lambda_b)/4$, $\lambda_1 := (\lambda_a + 3\lambda_b)/4$ within the wavelength interval $\lambda \in [\lambda_a, \lambda_b]$ of interest. The required continuous wavelength dependence is then (approximately) obtained by interpolation of the matrices K, i.e. as $K(\lambda) \approx K_{int}(\lambda) = K_0 + ((\lambda - \lambda_0)/(\lambda_1 - \lambda_0))(K_1 - K_0)$ where only $K_0 = K(\lambda_0)$ and $K_1 = K(\lambda_1)$ have to be computed explicitly. Finally one solves Eq. (12) for $\boldsymbol{u}(\lambda)$ with $K(\lambda)$ replaced by $K_{int}(\lambda)$. Extension to higher interpolation orders is obvious.

All spectral results shown in the following sections rely on this approximation with linear interpolation. The comparison with a directly computed scan in Section 3 shows that, for the present parameter set, the linear scheme is sufficient to obtain good qualitative and quantitative results.[2] For all other examples, the approximation is at least roughly checked at the wavelengths corresponding to the field plots (computed directly) that accompany the spectral scans.

Note that the interpolation does not necessarily conserve specific matrix properties. Hence, while it works well at the level of the original matrix K, the scheme is not applicable to the matrices in Eq. (12), at least not if a linear solver is employed that relies on the positivity of the system matrix [22], as in our present implementation.

Care must be taken that the interpolation is applied to continuous, slowly varying quantities only. For the formulation of Section 2.2 this implies that the approximate angular mode order κ must be selected uniformly over the entire wavelength interval (i.e. with Eq. (4) applied for a central target wavelength). The angular dependence is then captured by a moderately more pronounced variation of the amplitude $c(\theta)$.

Dispersion can be included straightforwardly into the present frequency domain model by describing the appropriate wavelength dependence of the refractive index values. For well behaved dispersion properties an interpolation scheme as above, if necessary of higher order, should be able to cover that additional wavelength variation as well.

3 Single ring filter

The single ring with two bus waveguides of Figure 1 serves as a constituting element for the circuits considered in the following sections. A parameter set from [19, 14] has been transferred to the more familiar wavelength region around $1.56\,\mu$m. The spectral scan in Figure 2 agrees well with the curves based on "conventional" CMT and also with the numerical FDTD results if [19, 14]. One also observes a reasonable agreement between the directly computed spectral properties and the outcome of the interpolation procedure of Section 2.3. As expected, the deviations increase at the ends of the interval of interest $\lambda \in [1.52, 1.63]\,\mu$m.

Beyond the mere power transfer properties, the HCMT model permits to assemble approximations to the full optical field. Figure 3 illustrates the field at the central resonance. So far these are pure traveling waves; any ripples that might appear in the plot of $|E_y|$ are thus attributable to sampling effects. For excitation in the top left port one observes a slightly larger intensity in the right half of the cavity, corresponding to a certain amount of non-resonant power transfer from the upper to the lower bus waveguide. This must thus be considered a strongly coupled configuration, also confirmed by the off-resonance levels of dropped power in Figure 2.

---

[2] One might observe that this interpolation process is quite analogous to the usual analytical evaluation of parametric CMT models [6], where one takes into account first or second order wavelength derivatives of effective mode indices and neglects the wavelength
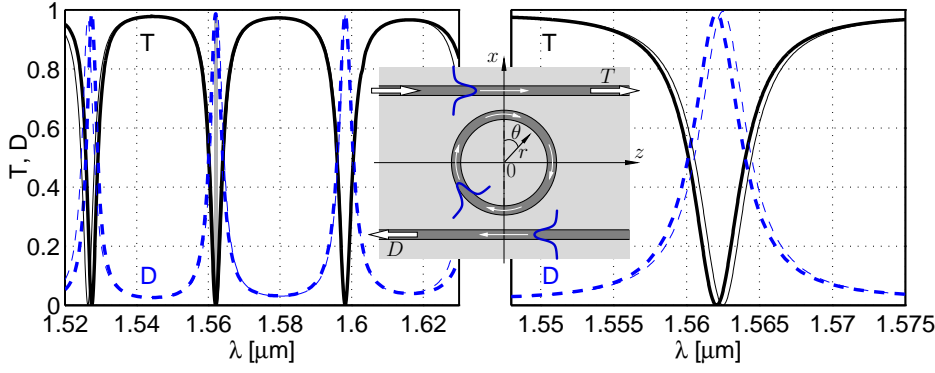
Figure 2: Power spectrum of the single ring filter as introduced in Figure 1, relative guided transmitted T and dropped optical power D versus the vacuum wavelength λ. Bold curves: direct computation; thin lines: interpolated spectral scan according to the procedure of Section 2.3.
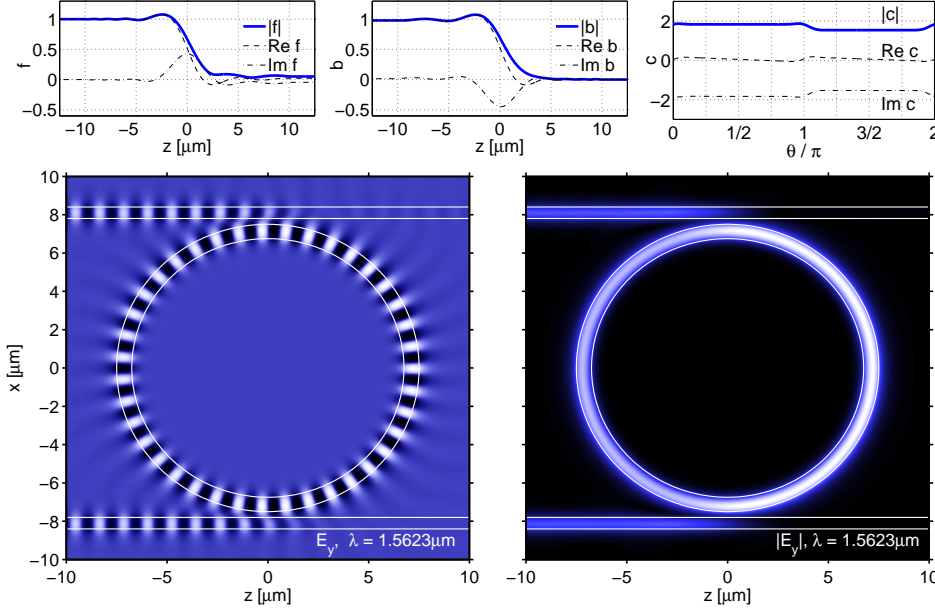

Figure 3: For the single ring filter of Figure 2: resonance at $\lambda = 1.5623\,\mu m$. Top row: coupled mode amplitudes $f(z)$, $b(z)$, and $c(\theta)$ associated with the waves in the upper and lower bus channel, and with the cavity mode, respectively. Bottom: time snapshot of the physical electrical field and field modulus, principal component E_y of the TE polarized waves.

Although no explicit analytic expressions for the amplitude functions are generated, one can at least inspect the numerical solutions of the CMT formalism for the coupled mode amplitudes. The wave interaction in the regions of closest approach $z \approx 0$, $\theta \approx 0, \pi$ of the bent and straight channels becomes apparent. Here the overlap of the nonorthogonal contributions to the optical field is most pronounced, hence it is not surprising that the levels of $|f|$ or $|b|$ exceed 1 in these regions. In-between, the slight slope of the curves for Rec and Imc reinstates the actual (complex) phase propagation constant of the bend mode after the replacement $\gamma \rightarrow \kappa$ as explained in Section 2.1. The attenuation of the bend mode is not visible, the level $|c|$ appears to be constant outside the interaction regions. Note that these curves are computed for the specific resonant state of the full device, hence they differ from plots of the spatial evolution of coupled mode amplitudes in the bend-straight coupler structures of [14]. In principle the reasoning of [14] on the extraction of modal output amplitudes by overlap evaluation applies here as well; however, since the amplitudes are not used here for subsequent computations we do not further elaborate this issue.

4 Coupled resonator optical waveguides

Chains of evanescently coupled ringresonators have attracted recent interest, as a means of channeling of optical power over the path of the resonators, but also for interest in their time delay properties [23, 24, 25]. Here we employ a series of coupled resonator optical waveguides (CROWs) with growing length to demonstrate the ability of the HCMT to cover also the ring-to-ring coupling without any further heuristics. So far the model remains restricted to unidirectional wave propagation.

Apart from the orientation and positioning of the bus cores, the field template now includes a bend mode profile with properly positioned origin and alternately clockwise and anticlockwise propagation direction for each of

dependence of coupling coefficients.

the cavity rings in the series. The computational window has been enlarged correspondingly. For upward guided wave excitation in the left channel, the drop output is being detected in the upper (even number of cavities) or lower outlet of the bus waveguide at the right.
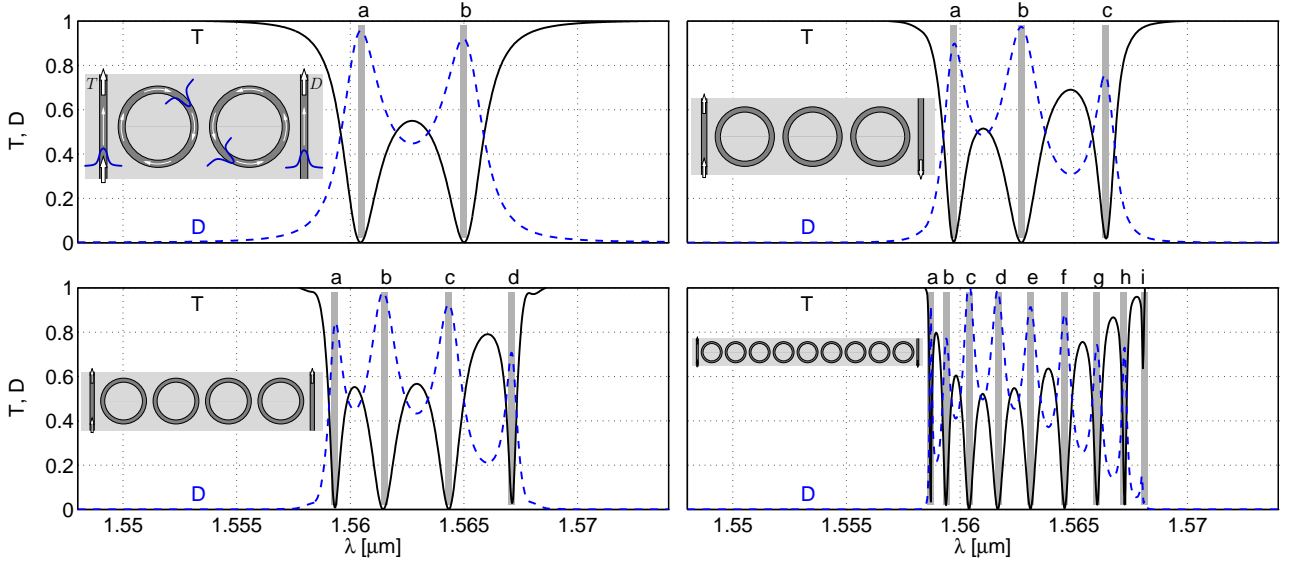

Figure 4: Spectral properties of CROW structures with 2, 3, 4, and 9 evanescently coupled rings, relative directly transmitted T and dropped guided optical power D.

Figure 4 shows the spectral response of CROWs built from cavities with the parameters of the ring of Section 3. The features recur with the free spectral range of the individual cavity. Hence, for the CROWs, we concentrate on a wavelength range $\lambda \in [1.55, 1.57]\,\mu$m that includes only one resonance of the single ring device at $\lambda = 1.5623\,\mu$m. When compared to Figure 2, one observes a sharpening of features with growing number of rings, manifested e.g. by the much smaller off-resonance drop levels. The dip/peak of the single ring device splits into a series, corresponding to the supermodes of the CROW structures. The related resonant fields can be inspected in Figure 5. A systematics akin to standard Fourier harmonics is clearly recognizable. "Nodes" are realized either as fields with opposite symmetry on both sides of a gap (not evident from the present plots, actual physical fields would be required), or by entire rings in an "off"-state.
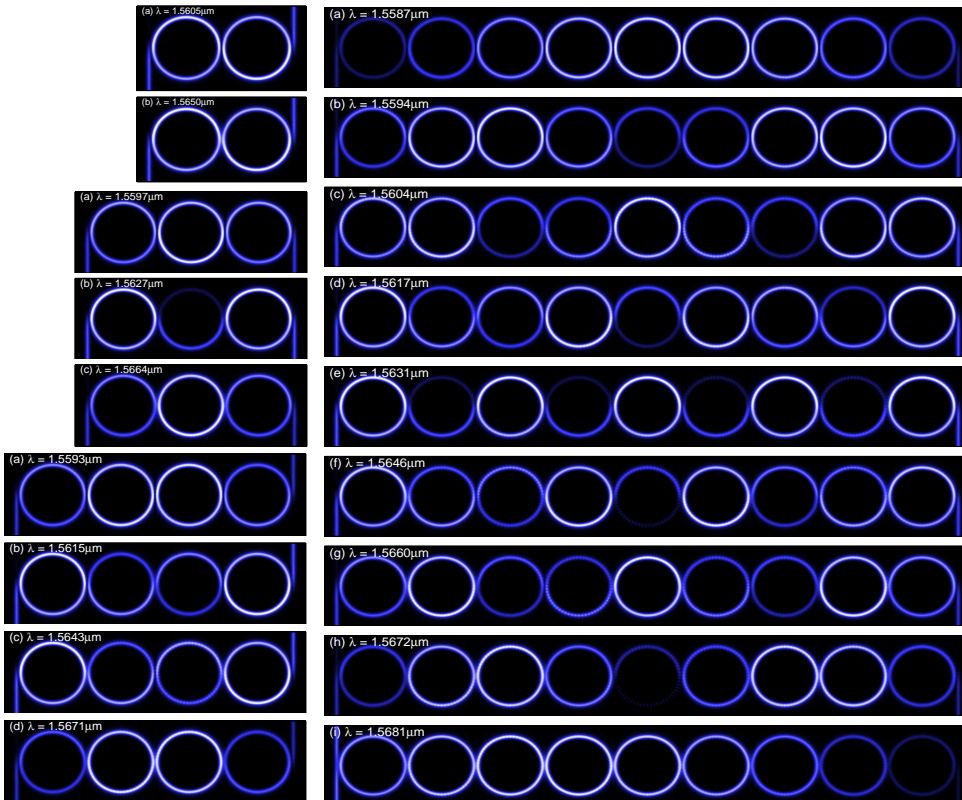

Figure 5: Field patterns associated with the resonances as indicated (letters) in the spectra of Figure 4, the plots show the absolute value of the principal electric component of the TE fields.

7

5 Parallel rings

Now we place two of the former rings such that each interacts with both bus cores as well as with the other cavity. The direct coupling between the rings can be expected to excite bidirectional wave propagation in both rings, and consequently also in the access waveguides. Therefore the field template includes prototypes for the forward and backward propagating guided waves of the upper and lower straight channels, and prototypes for clockwise and anticlockwise traveling bend modes of both cavities. Figure 6 shows the response of a device in a spectral range around the single-ring resonance at $1.5623\,\mu$m.
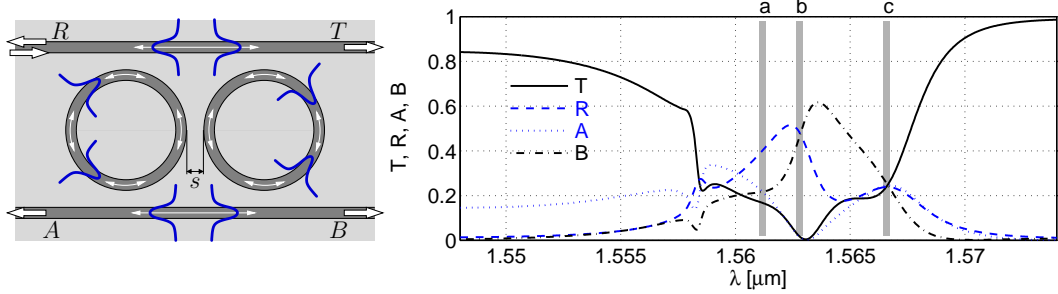
Figure 6: *Two microrings coupled in parallel. Parameters are as in Figure 1, with a gap $s = 0.25\,\mu$m between the rings. Upon excitation with wavelength λ in the upper left port, the power is distributed to the outlets T, R, A, and B.*

In contrast to the sequential arrangement in Section 4 here we see broadened features, probably due to stronger direct, also non-resonant, interaction. Possibly other regimes can be realized with different parameters. The cavity gap s has been adjusted such that at a specific wavelength the input power is distributed equally among all four output ports. Corresponding fields are shown in part (c) of Figure 7.
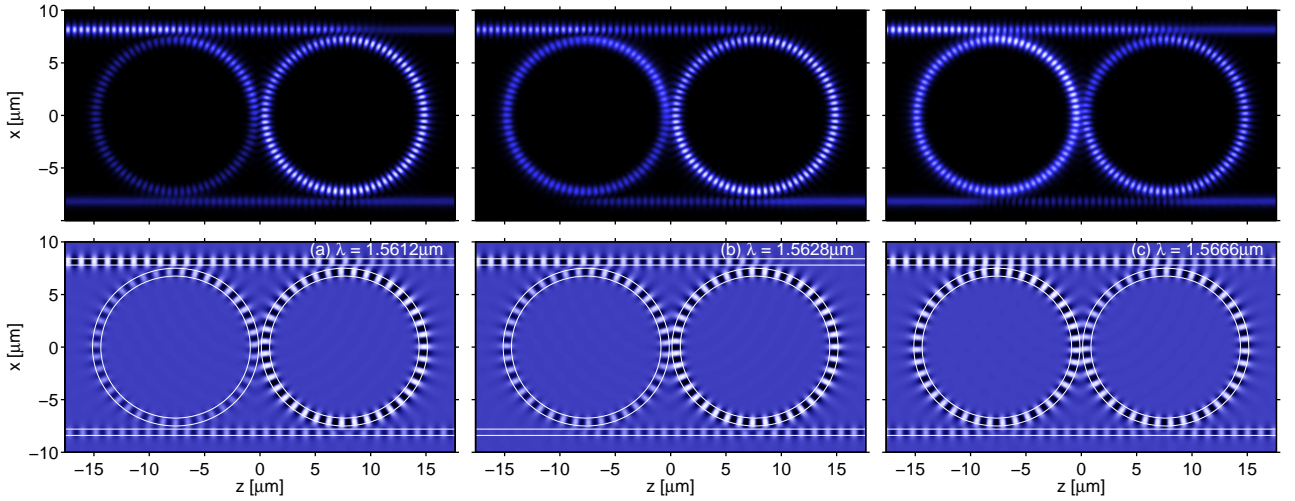

Figure 7: *Field patterns (absolute values and time snapshots of the principal electric field component) observed for the parallel ring configuration of Figure 6 at three selected wavelengths. The overall phase for the plots in the lower row has been chosen (roughly) such that the maximum wave amplitude becomes visible.*

Among the manifold spectral features we selected two other wavelengths for field illustrations: In configuration (a) about 0.4 of the unit input power is reflected, while the remainder is roughly equally distributed among the other three outlets. The field plots show a major light path that consists of the upper right quarter of the left resonator, followed by the three lower and right quarters of the right resonator and the central piece of the upper straight waveguide, i.e. a loop that includes pieces of both resonators. A similar loop, though with higher intensity in the other parts of the left cavity, is realized in configuration (b), where the backward drop A and the direct transmission T are suppressed almost entirely, while roughly half of the input power is reflected (R) and dropped forward (B).

In this case the ripples in the $|E_y|$-plots indicate standing waves caused by bidirectional mode interference. Time animations of the physical E_y-fields, however, reveal a mixture of standing and traveling waves. Hence, while in principle the symmetry-related supermode model of [26, 27, 28] should be applicable, not all spectral features might be easily explainable for the present structure with quite strong interaction.

6 R3 resonator

Next we consider the configuration of Figure 8: Three rings are placed on the corners of a equilateral triangle, excited through a single straight bus channel next to one of the rings. The entire structure is symmetric with respect to the central horizontal axis. A motivation could be found in the photonic molecules of e.g. [29, 30]. Here, however, the concepts have been realized with much larger rings, corresponding to whispering gallery resonances of higher order, and we are considering the structure explicitly with external guided wave excitation, not the states of isolated molecules. Nevertheless these will play a role in the brief discussion below. This could be seen as an example where a conventional scattering matrix model based on a division of the structure into separate coupling regions with well defined outlets seems to be neither appropriate nor convenient.
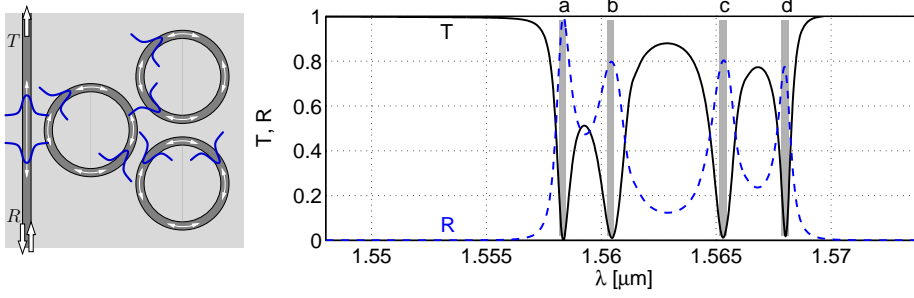

Figure 8: A triangular arrangement of coupled rings, accessed by a single bus waveguide. Transmission T and reflectivity R versus the vacuum wavelength λ.

Obviously the HCMT model has to allow for bidirectional wave propagation again. The template now includes up- and downwards propagating modes for the bus channel, and clock- and anticlockwise traveling bend modes for each of the three rings, in total eight unknown functions. Their FE discretization (equidistant, first order 1-D elements; bus: $x \in [-17.65, 17.65]\,\mu$m, 89 coefficients; rings: $\theta \in [0, 2\pi]$, 118 unknowns) leads to a system of equations (10) of dimension 886. The overlaps K_{lk} are evaluated on an integration window of $(x, z) \in [-17.65, 17.65] \times [-2.5, 33.1]\,\mu$m^2. Our parameters are as in Figure 1, with equal gaps g between all respective cores at the points of closest approach. Figures 8 and 9 summarize the outcome of these simulations.
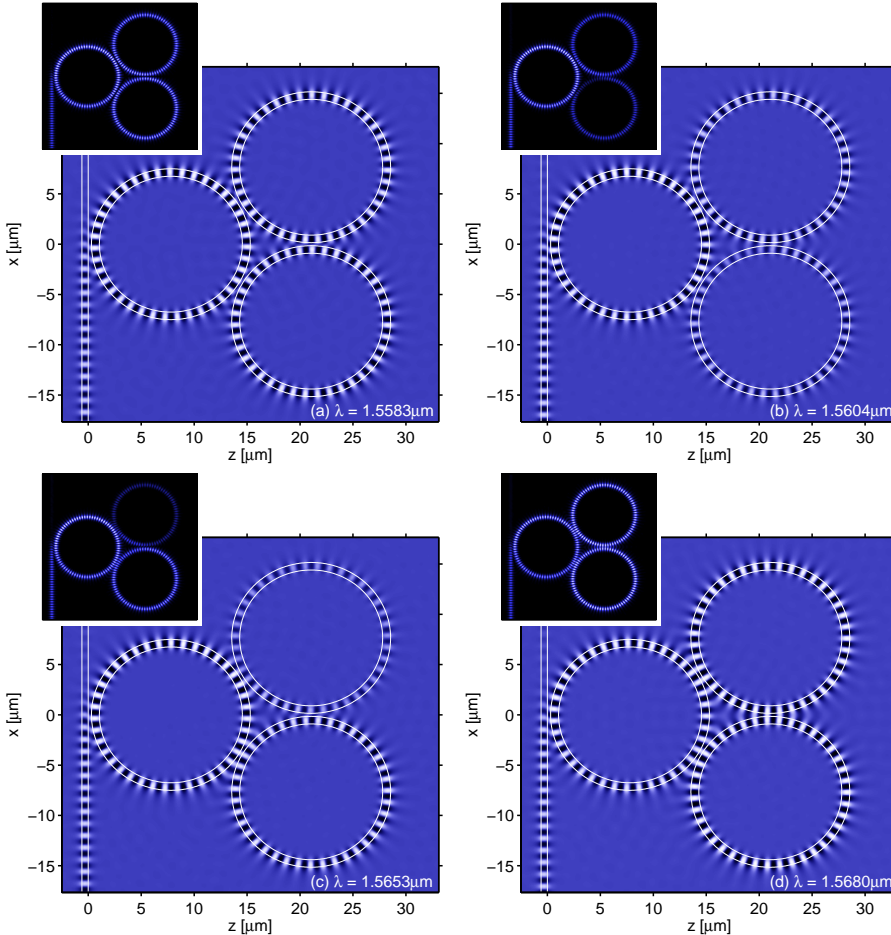

Figure 9: Resonant fields (absolute values and time snapshots of the principal electric field component) supported by the triple ring configuration of Figure 8.

The original single-ring resonance splits into four features with high reflectivity and almost canceling transmission. In particular at wavelength $\lambda = 1.5583\,\mu$m (a), the structure acts as a good reflector for guided waves. Animations of the stationary, time harmonic fields show almost purely standing waves with simultaneous large amplitudes in all parts of the structure. The (rough) symmetries of the excited "supermodes" can be understood by inspecting the field levels and signs in adjacent cores of the three central inter-cavity coupling regions: One recognizes a field that is antisymmetric with respect to the division lines of all three couplers (a), one that is symmetric with respect to the horizontal axis $x = 0$ but antisymmetric over the two angled division lines (b), then a field that is antisymmetric with respect to $x = 0$ but symmetric over the two angled division lines (c), and finally the field (d) that is symmetric over all three couplers.

7 Slit ring resonator

The whispering gallery modes (WGMs) of a rotationally symmetric cavity are twice degenerate [31]; the degeneracy is related to the arbitrariness in the choice of the origin of the angular coordinate in a description in polar coordinates. Introducing a perturbation, e.g. in the form of an evanescently coupled bus waveguide, can be expected to lift this degeneracy. One thus would expect to see separate peaks in the transmission or reflection curves, each associated with the excitation of a WGM of different symmetry. In principle our model should be able to capture that effect as well: the field template say for the single ring of Section 3 would have to be extended by counter-propagating waves. When carrying out the respective simulations, however, we received precisely the same answers as shown in the former plots, at least within our present accuracy limits.

This is confirmed by the arguments of [32], where this problem has been investigated by a parametric analytical model. For all reasonable parameters (of the idealized model systems) the wavelength shifts due to the degeneracy lifting are obscured by the natural width of the resonance peaks. The authors propose to look at a different structure that enlarges the effect: an artificial, somewhat stronger reflector is introduced into the resonator, which does not influence the functioning of the couplers.[3] We adopt this concept as our last example.

The reflector is realized as a slit in the ring cavity of our standard single ring device. Figure 10 shows a schematic. For simplicity only one access waveguide is considered, such that the respective theory of [32] becomes applicable. The structure is quite similar to the concept investigated in [34]. Note, however, that here we can carry out ab-initio simulations; in principle the results provide a quantification of those models.
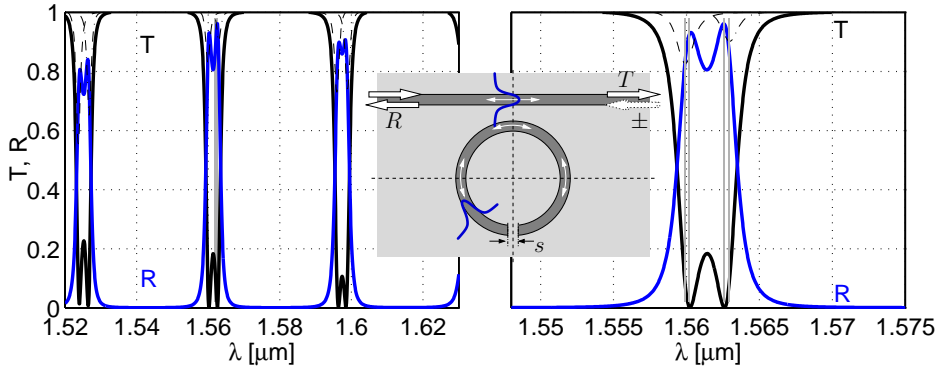

Figure 10: Ring resonator with a slit. Transmission T and reflection R versus wavelength λ. Parameters are as in Figure 1, with a slit $s = 0.2\,\mu$m. Bold continuous lines: excitation in the left port only; thin lines, mostly shadowed: symmetric (dashed) and antisymmetric excitation (dash-dotted) in both ports.

In principle, the HCMT model can be applied just as before, where the template now includes bidirectional waves for both the cavity and the bus core. The slit merely leads to a slightly modified dielectric permittivity ϵ in Eqs. (7) and (9), respectively. Nevertheless, according to Figure 10, it affects the spectral response significantly. We focus on the thick curves first, that show the relative transmission and reflection due to an excitation in only one of the outlets. Resonances occur still at the positions and with the free spectral range as for the continuous ring in Figure 2, but appear now as doublets. At the extreme configurations, the transmission vanishes almost entirely, most of the inserted power is reflected. The two central plots of Figure 11 allow to inspect the symmetry properties of the associated fields. One observes almost purely standing waves in the cavity, with a field pattern that is roughly symmetric (lower wavelength) or antisymmetric with respect to the vertical axis.

Apparently, the slit here acts as a sufficiently strong reflector to well separate the resonances associated with the WGMs of the same order, but with different symmetry. If this would not have been the case, one could

---

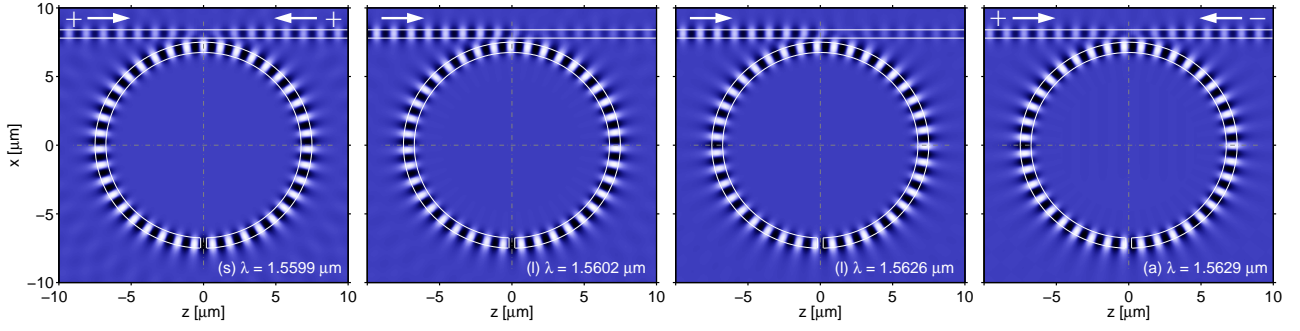[3]This might well relate to actual physical effects, e.g. to a pronounced surface roughness [33, 32].

Figure 11: *Slit ring resonator, field pattern associated with the extremal configurations indicated in Figure 10. (s): symmetrical excitation from both the left and right ports, (l): an incoming wave from the left only, two different wavelengths close to the (s) and (a) resonances, (a): antisymmetric excitation from left and right.*

have followed the recipe of [32] to excite exclusively one WGM with definite symmetry, by prescribing optical input with the respective symmetry in both the left and right outlet. The overall solution then obviously shares this symmetry. This experiment can also be easily repeated within the HCMT model by switching the given coefficient related to the last finite element of the backward mode in the upper channel from 0 to 1, then to -1. Figure 10 includes two related curves. The output power received at both ports is always identical; resonances show up through the cavity losses (lossy bend modes play a role). These resonances appear at different positions for excitation with different symmetry, very close to the former two peaks of the same symmetry. The small deviation could be attributed to the influence that the "other" WGM still might have for single-side excitation close to the eigenfrequency of one of the WGMs.

To quantify the former findings, we apply the theory of [32]. The analytical model predicts a wavelength shift

$$\Delta\lambda \approx \frac{\lambda^2}{2\pi^2 N_{\mathrm{r}} R}\frac{|\rho|}{|\tau|} = \frac{\lambda}{\pi\gamma R}\frac{|\rho|}{|\tau|} \tag{13}$$

between the resonances observed for symmetric and asymmetric excitation in both the left and right outlet of the bus channel. Here ρ and τ are the amplitude reflectance and transmittance of the reflector for guided wave incidence, $N_{\mathrm{r}} = \mathrm{Re}\gamma/k$ is the real part of the effective index associated with the bend mode of the cavity, and R is the related cavity radius.

Rather than viewing the ratio $|\rho/\tau|$ as a fit parameter, one could estimate it from first principles as well, i.e. as the modal reflection that the guided mode of an analogous straight channel experiences when encountering a slit as in our cavity. The HCMT approach can also applied to this latter problem, together with a reference calculation (quadridirectional eigenmode propagation, QUEP [35]); Figure 12 compares the corresponding field data. At the central wavelength $\lambda = 1.5614\,\mu$m of the resonance the reference simulation gives values of $|\rho|^2 = 0.062$, $|\tau|^2 = 0.905$ for the relative transmission and reflection of the guided TE mode. The HCMT model is reasonably close with values of $|\rho|^2 = 0.073$, $|\tau|^2 = 0.927$. Note that the scattered waves are entirely neglected in the (here power conservative) HCMT simulation of the slab hole.
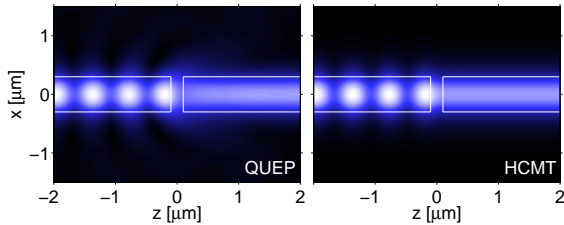

Figure 12: *Straight waveguide with a hole, a guided wave enters from the left and is partly reflected; rigorous reference calculation (QUEP, [35]) and HCMT model. The plots show the absolute value $|E_y|$ of the principal electric field component of the TE waves.*

Assuming that the outcome of the HCMT model for the bend mode reflection at the slit in the ring is not too different, with the values $R = 7.5\,\mu$m and $N_{\mathrm{r}} = 1.294$ (hardly any change within the 5 nm interval that covers the central resonance in Figure 10), Eq. (13) predicts a wavelength shift of $\Delta\lambda = 3.6$ nm. This agrees reasonably with the difference of about 3 nm observed in Figures 10 and 11. Hence the present HCMT simulations are consistent with the analytical description of [32].

8 Concluding remarks

While being related to standard analytic parametric microresonator models, our hybrid approach shows certain advantages: No free parameters appear, full field information is available, and the technique is quite flexible as long as a physically reasonable field template can be established and handled conveniently. The price is a somewhat higher computational effort than what would be required for the evaluation of pure analytic equations, and a number of numerical parameters (computational window & intervals, stepsizes) that need adjustment. Being computationally significantly cheaper than any pure numerical scheme, the HCMT approach is certainly also more restricted in its range of applicability, and convergence can be guaranteed up to the limits of the initial template only. One might thus see this as an intermediate method between an analytic treatment on the one hand, and a general rigorous numerical technique on the other hand.

The present implementation and all examples are restricted to 2-D. The formulation of the approach in Section 2, however, applies to 3-D configurations as well. An HCMT version in 3-D would have to rely on numerically computed modes of straight and bent channels, just as in [15]. While the size of the systems (11), (12) remains about the same as in 2-D, the computational cost will depend largely on the amount of sophistication that is invested into the evaluation of the modal element overlaps (9). Hence, 3-D HCMT simulations on circuits as in our examples won't be exactly fast, but should be sufficiently efficient for actual device design.

Our main purpose has been the demonstration of the capabilities of the modeling approach. Each of the examples addressed other and increasingly complex aspects of the HCMT formalism. The discussion of the physical properties of these systems could only be touched; the present implementation of the HCMT formalism constitutes a convenient basis for further numerical experiments.

Note that we have looked here at a pure frequency domain reasoning (cf. Eqs. (7)). The fields are built of bend modes (2) which usually do not fit into the circular cavities, i.e. differ in amplitude and phase at the angular origin after a 2π round trip. Only the interaction with the bus waveguides, or with other cavities, enables the formation of resonances through a non-constant amplitude $c(\theta)$. The resonances are thus to be attributed to the entire system, not to the cavity alone. As an alternative one could try to establish a model based on the whispering gallery modes of the circular cavities [36], i.e. on fields with complex frequency and integer angular wavenumber. Similar to [17], the HCMT template would then include the bus modes with their varying amplitudes, together with a series of whispering gallery modes of the cavity that fall in the wavelength interval of interest, each multiplied by a single variable coefficient. Implementation and evaluation of that approach is under way.

Acknowledgments

References

[1] M. Bertolotti, A. Driessen, and F. Michelotti, eds., *Microresonators as building blocks for VLSI photonics*, vol. 709 of AIP conference proceedings (American Institute of Physics, Melville, New York, 2004).

[2] I. Chremmos, N. Uzunoglu, and O. Schwelb, eds., *Photonic Microresonator Research and Applications*, Springer Series in Optical Sciences, Vol. 156 (Springer, London, 2010).

[3] L. F. Stokes, M. Chodorow, and H. J. Shaw, "All-single-mode fiber resonator," Optics Letters **7**, 288–290 (1982).

[4] K. Okamoto, *Fundamentals of Optical Waveguides* (Academic Press, SanDiego, 2000).

[5] A. Yariv, "Universal relations for coupling of optical power between miroresonators and dielectric waveguide," Electronic Letters **36**, 321–322 (2000).

[6] M. Hammer, K. R. Hiremath, and R. Stoffer, "Analytical approaches to the description of optical microresonator devices," in "Microresonators as building blocks for VLSI photonics," , vol. 709 of AIP conference proceedings, M. Bertolotti, A. Driessen, and F. Michelotti, eds. (American Institute of Physics, Melville, New York, 2004), pp. 48–71.

[7] D. J. W. Klunder, E. Krioukov, F. S. Tan, T. van der Veen, H. F. Bulthuis, G. Sengo, C. Otto, H. J. W. M. Hoekstra, and A. Driessen, "Vertically and laterally waveguide-coupled cylindrical microresonators in Si_3N_4 on SiO_2 technology," Applied Physics B **73**, 603–608 (2001).

[8] D. J. W. Klunder, M. L. M. Balistreri, F. C. Blom, H. J. W. M. Hoekstra, A. Driessen, L. Kuipers, and N. F. van Hulst, "Detailed analysis of the intracavity phenomena inside a cylindrical microresonator," Journal of Lightwave Technology **20**, 519–529 (2002).

[9] D. J. W. Klunder, F. S. Tan, T. van der Veen, H. F. Bulthuis, G. Sengo, B. Docter, H. J. W. M. Hoekstra, and A. Driessen, "Experimental and numerical study of SiON microresonators with air and polymer cladding," Journal of Lightwave Technology **21**, 1099–1110 (2003).

[10] C. Vassallo, *Optical Waveguide Concepts* (Elsevier, Amsterdam, 1991).

[11] D. G. Hall and B. J. Thompson, eds., *Selected Papers on Coupled-Mode Theory in Guided-Wave Optics*, vol. MS 84 of *SPIE Milestone Series* (SPIE Optical Engineering Press, Bellingham, Washington USA, 1993).

[12] D. R. Rowland and J. D. Love, "Evanescent wave coupling of whispering gallery modes of a dielectric cylinder," IEE Proceedings, Pt. J **140**, 177–188 (1993).

[13] M. K. Chin and S. T. Ho, "Design and modeling of waveguide-coupled single-mode microring resonators," Journal of Lightwave Technology **16**, 1433–1446 (1998).

[14] K. R. Hiremath, R. Stoffer, and M. Hammer, "Modeling of circular integrated optical microresonators by 2-D frequency-domain coupled mode theory," Optics Communications **257**, 277–297 (2006).

[15] R. Stoffer, K. R. Hiremath, M. Hammer, L. Prkna, and J. Čtyroký, "Cylindrical integrated optical microresonators: Modeling by 3-D vectorial frequency domain coupled mode theory," Optics Communications **256**, 46–67 (2005).

[16] M. Hammer, "Hybrid analytical / numerical coupled-mode modeling of guided wave devices," Journal of Lightwave Technology **25**, 2287–2298 (2007).

[17] M. Hammer, "Chains of coupled square dielectric optical microcavities," Optical and Quantum Electronics **40**, 821–835 (2009).

[18] K. R. Hiremath, M. Hammer, R. Stoffer, L. Prkna, and J. Čtyroký, "Analytical approach to dielectric optical bent slab waveguides," Optical and Quantum Electronics **37**, 37–61 (2005).

[19] K. R. Hiremath, *Coupled Mode Theory Based Modeling and Analysis of Circular Optical Microresonators* (University of Twente, Enschede, The Netherlands, 2005). Ph.D. Thesis.

[20] M. Hammer, "METRIC — Mode expansion tools for 2D rectangular integrated optical circuits," http://www.math.utwente.nl/∼hammerm/Metric/.

[21] K. R. Hiremath, "CIRCURS — Circular resonator simulator," http://www.math.utwente.nl/aamp/FormMem/Hiremath/circurs/.

[22] W. H. Press, S. A. Teukolsky, W. T. Vetterling, and B. P. Flannery, *Numerical Recipes in C, 2nd ed.* (Cambridge University Press, 1992).

[23] A. Yariv, Y. Xu, R. K. Lee, and A. Scherer, "Coupled-resonator optical waveguide: a proposal and analysis," Optics Letters **24**, 711–713 (1999).

[24] B. E. Little, S. T. Chu, P. P. Absil, J. V. Hryniewicz, F. G. Johnson, F. Seiferth, D. Gill, V. Van, O. King, and M. Trakalo, "Very high-order microring resonator filters for WDM applications," IEEE Photonics Technology Letters **16**, 2263–2265 (2004).

[25] F. Morichetti, A. Melloni, A. Breda, A. Canciamilla, C. Ferrari, and M. Martinelli, "A reconfigurable architecture for continuously variable optical slow-wave delay lines," Optics Express **15**, 17273–17281 (2007).

[26] C. Manolatou, M. J. Khan, S. Fan, P. R. Villeneuve, H. A. Haus, and J. D. Joannopoulos, "Coupling of modes analysis of resonant channel add-drop filters," IEEE Journal of Quantum Electronics **35**, 1322–1331 (1999).

[27] S. Fan, P. R. Villeneuve, J. D. Joannopoulos, M. J. Khan, C. Manolatou, and H. A. Haus, "Theoretical analysis of channel drop tunneling processes," Physical Review B **59**, 15882–15892 (1999).

[28] M. J. Khan, C. Manolatou, S. Fan, P. R. Villeneuve, H. A. Haus, and J. D. Joannopoulos, "Mode-coupling analysis of multipole symmetric resonant add/drop filters," IEEE Journal of Quantum Electronics **35**, 1451–1460 (1999).

[29] S. V. Boriskina, "Spectrally engineered photonic molecules as optical sensors with enhanced sensitivity: aproposal and numerical analysis," Journal of the Optical Society of America **23**, 1565–1573 (2006).

[30] E. I. Smotrova, A. I. Nosich, T. M. Benson, and P. Sewell, "Threshold reduction in a cyclic photonic molecule laser composed of identical microdisks with whispering-gallery modes," Optics Letters **31**, 921–923 (2006).

[31] E. I. Smotrova, A. I. Nosich, T. M. Benson, and P. Sewell, "Cold-cavity thresholds of microdisks with uniform and nonuniform gain: Quasi-3-D modeling with accurate 2-D analysis," IEEE Journal of Selected Topics in Quantum Electronics **11**, 1135–1142 (2005).

[32] J. Čtyroký, I. Richter, and M. Šiňor, "Dual resonance in a waveguide-coupled ring microresonator," Optical and Quantum Electronics **38**, 781–797 (2006).

[33] M. Borselli, T. J. Johnson, and O. Painter, "Beyond the Rayleigh scattering limit in high-Q silicon microdisks: theory and experiment," Optics Express **13**, 1515–1530 (2005).

[34] Y. M. Kang, A. Arbabi, and L. L. Goddard, "A microring resonator with an integrated bragg grating: a compact replacement for a sampled grating distributed bragg reflector," Optical and Quantum Electronics **41**, 689–697 (2010).

[35] M. Hammer, "Quadridirectional eigenmode expansion scheme for 2-D modeling of wave propagation in integrated optics," Optics Communications **235**, 285–303 (2004).

[36] L. Prkna, J. Čtyroký, and M. Hubálek, "Ring microresonator as a photonic structure with complex eigenfrequency," Optical and Quantum Electronics **36**, 259–269 (2004).